FRACTURE CHARACTERISTICS OF TAILINGS-BASED GEO-POLYMER INCLUDING CLASS F FLY ASH ACCORDING TO MODE I LOADING CIRCUMSTANCES

Vipin Gupta, M.Tech Scholar in Department of Civil Engineering, Faculty of engineering & Technology**. Email Id:** vipingupta8201@gmail.com
Satish Parihar, Associate Professor of Civil department of Engineering, Faculty of engineering & Technology **Email Id:** satishparihar.fet@ramauniversity.ac.in
Vaibhav Dubey, Assistant Professor of Civil department of Engineering, Faculty of engineering & Technology **Email Id:** vaibhavdube.fet@ramauniversity.ac.in

Abstract: Geo-polymer is formed by alkali-activation of mine tailings (MTs) is a possible substitute for Portland cement concrete in construction. It exhibits similar brittle qualities to rocks and concrete. The pure met kaolin did not include enough amorphous aluminosilicates to enhance alkali activation. Adding materials containing crystalline aluminosilicates is crucial to enhance reactivity, modify geopolymeric cell structures, and enhance cementitious characteristics. This research used class F fly ash (FA) as an amorphous supplement to boost alkali reactivity and improve mechanical and fracture qualities. FA and MTs were first identified by a range of laboratory tests, including conventional geotechnical testing, X-ray diffraction (XRD) analysis, and scanning electron microscopy with Energy dispersive X-ray analysis (SEM-EDS) analysis. Geo-polymer samples were produced by activating mixes of fly ash and metakaolin with 10 M sodium hydroxide solutions at a moisture ratio of 16%. The samples were subsequently cured for 7 days at a slightly elevated temperature. Semi-circular bending tests (SCB) were performed to assess how various FA additions affect the fracture behaviour of the geopolymer. Additionally, digital image correlation (DIC) was used to analyze the strain behaviors and fracture propagation features of the geo-polymer. The impact of FA additives on crack tip opening displacement (CTOD) and fracture process zone (FPZ) was also examined. Results indicate that under the current curing conditions, the addition of class F additives Formic acid does not enhance the potassium ion conductivity at lower concentrations but does increase it at greater concentrations. The connection between microscopic observations and fracture characteristics of the geopolymer containing FA was also examined.
Keywords: Geo-polymer Tailings of Gold Mines I break down characteristics Semi-circular bending test for Class F fly ash digital picture matching

1.0 Introduction

Mining operations produces waste residuals such as waste rocks or tailings on a regular basis, which may result in serious environmental problems. Several studies have described the developing practice of reusing aluminosilicate-rich tailings by alkaline activation to generate geopolymer. Geopolymers possess brittle qualities akin to concrete and rocks, making them suitable for usage in construction materials. Utilising tailings by alkali activation may minimise environmental effects and provide advantages. Like other geopolymers, tailings-based geopolymer is an environmentally friendly cement-like substance that depends on the alkaline activation of inorganic amorphous aluminosilicates. The often reported geopolymer binder consists of a significant quantity of crystalline aluminium silicates.

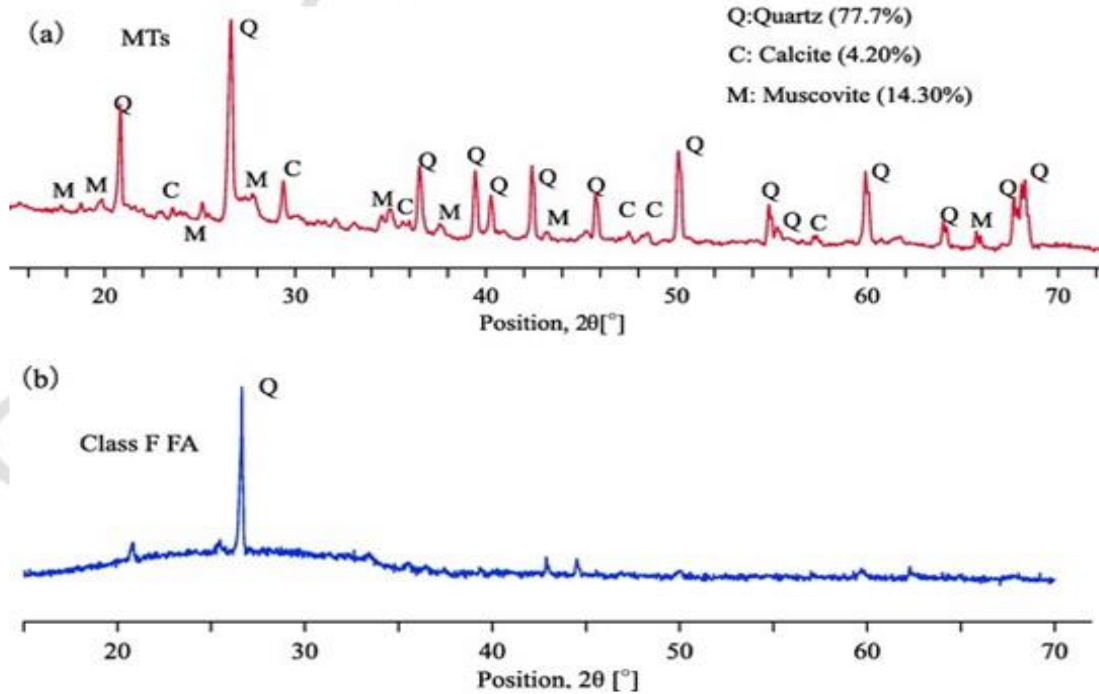Fig. 1. Diagram of MTs origins and the geotechnical properties

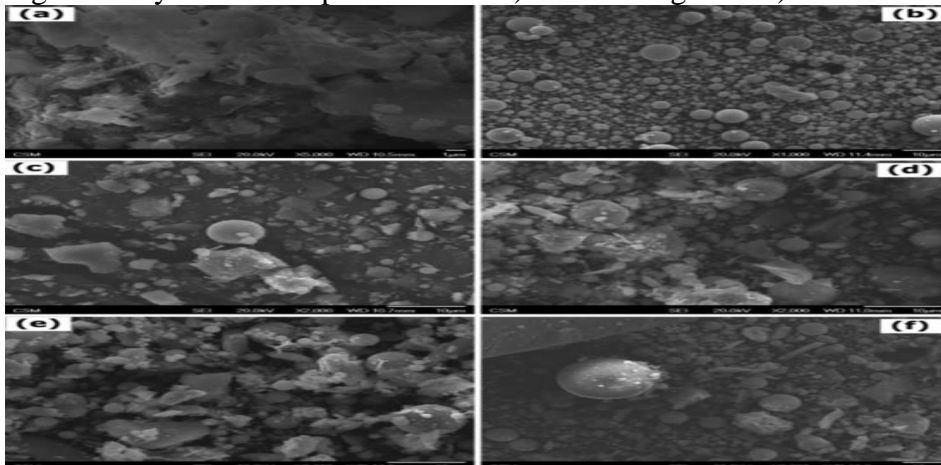Fig. 2. X-ray diffraction pattern of the a) mine tailings and b) class F FA Q-quartz; M-muscovite

Fig. 3. SEM micrographs of the raw material mixtures: a) raw mine tailings, b) fly-ash, c) 95 %MTs + 5 %FA, d) 90 %MTs + 10 %FA, e) 85 %MTs + 15 %FA, and f) 80 %MTs + 20 %FA

including fly-ash (FA), ground-grain blast furnace slag (GGBFS), or amorphous silica with enough alkaline constituents. FA, GG-BFS, and silica are often used raw materials including reactive aluminosilicates for geopolymer production [9–16]. The geopolymer is environmentally benign as it produces much lower carbon emissions compared to Portland cement concrete [17,18], while also having comparatively more durability.

Geopolymer is an inorganic substance typically created by alkaline activation of source materials abundant in aluminosilicates at temperatures below 100 °C. Kiventera et al. [19] said that MTs are often kept in garbage heaps for solids or in impoundment lakes for slurries. The impoundment was developed using tailing dams first erected using dykes made from materials imported from other locations. The tailing dams continued to expand as mineral processing activities progressed. The sedimentary soils settled to help raise the height of the existing dams. The ongoing daily generation of tailings is burdensome for their storage. The studies might focus on tailings storage or resource utilisation to reduce environmental consequences and provide advantages. Hence, creating strategies to repurpose the tailings is driven by the need to reduce both economic and environmental issues and alleviate storage constraints. Recently, the method of recycling solid MTs by compressing them into adobes was shown to be suitable for applications with lower strength requirements, although its applicability is restricted. It is necessary to investigate innovative methods for reusing the tailings. Aluminosilicate-rich MTs have been used to create geopolymer according to recent reports [22–26].
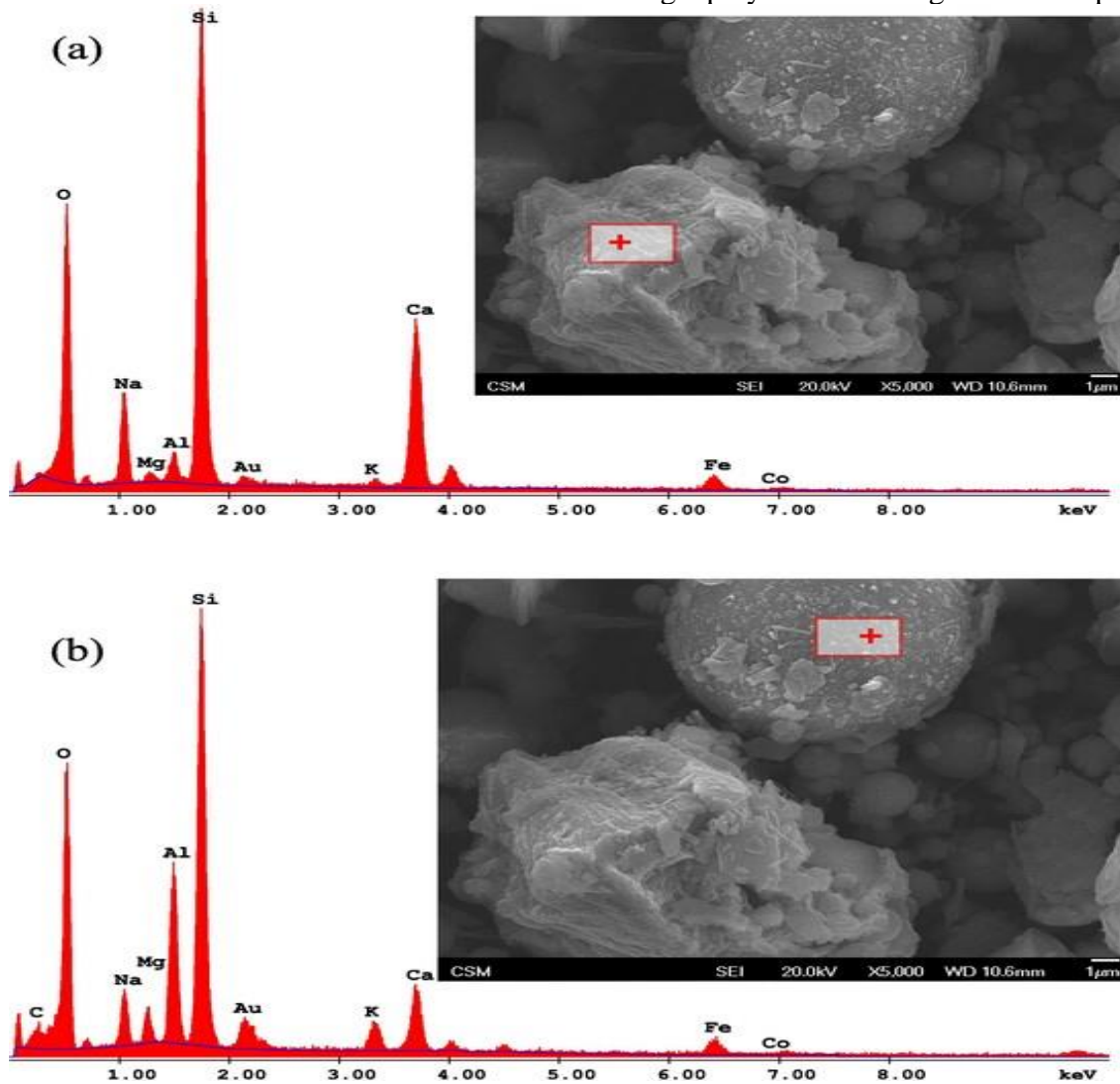

Fig. 4. SEM micrographs and EDS spectrum of a) MTs particles and b) FA particle

Nevertheless, pure metakaolins lack the necessary amount of reactive aluminosilicate (with a reactive Si: Al ratio often above 2) or enough amorphous aluminosilicate to impact mechanical strength. Thus, the addition of amorphous aluminosilicates was essential to modify the cell architectures for improved geopolymerization. Comprehensive research has been conducted, including other sources of amorphous aluminosilicates such fly ash, metakaolin, which silica fume, and slag, to enhance the mechanical properties of geopolymers [27–34]. Understanding the mechanical behaviours and fracture characteristics of geopolymers is crucial for their use in construction and building. Researchers have studied the flexural tensile properties of fly-ash-based geopolymer, as well as the use of admixtures such carbon fibre and rebars to improve its flexural behaviour. The study also examined the increase in splitting tensile strength of geopolymer based on MTs by performing Brazilian indirect tensile tests. Various researchers have examined the uniaxial compressive strengths (UCS) of the MTs-based geopolymer without admixtures, as shown in studies such as [32, 39, 40]. The tests were often used to study the mechanical properties of brittle building materials and widely studied in the analysis of rocks, ceramics, and regular concrete. Geopolymer, a typical brittle material, is susceptible to fracture failure, which may impact its performance and longevity. Commonly used methods to study the fracture behaviour of brittle materials include semi-circular bending tests, notch three point bending tests, and notch four point bending tests conducted on beams [20, 45–49]. Fracture toughness is a significant fracture property that may be determined using an empirical equation developed from experiments or Digital Image Correlation (DIC) research. The strain behaviours were typically derived using DIC analysis [20].
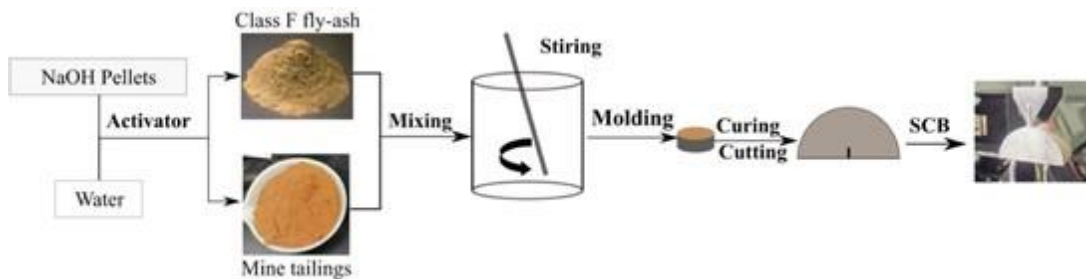

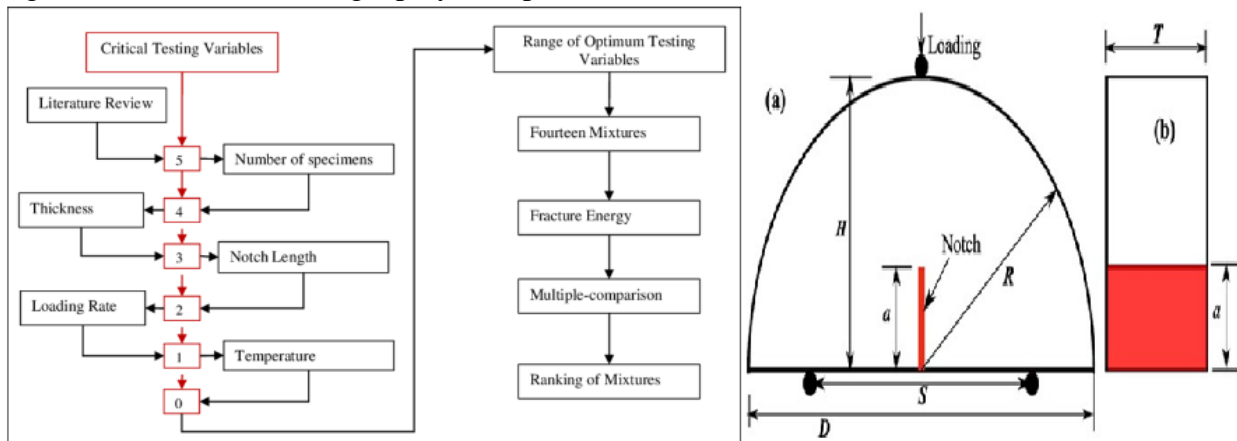Fig. 5. Procedures to make geopolymer specimens

Fig. 6. SCB specimens with different addition of fly-ash.

Geopolymer derived from tailings is suitable for building applications, namely as pavement bricks capable of withstanding pedestrian loads. Geopolymer bricks may have uneven settling, resulting in structural fractures. The study on the fracture characteristics of the tailings-based geopolymer was significantly restricted. The impact of additives on the mechanical and microscopic properties of the MTs-based geopolymer has not been investigated or recorded. The gold MTs used in this investigation had relatively low levels of aluminium and amorphous aluminosilicates. This work

used class F FA as amorphous aluminosilicates to modify the Si: Al ratio and improve reactivity for geopolymer production by alkaline activation. The effects of adding class F FA on the microscopic behaviours, mineralogical, and chemical characteristics of the geopolymer matrix were first studied by SEM/EDX and XRD analyses. The process of creating geopolymer by alkaline activation of metakaolin was explained. The semi-circular bending (SCB) tests were performed to study the mode I fracture behaviour and crack propagation of the geopolymer based on metakaolin (MTs) with class F fly ash (FA) added. The strain behaviours and fracture behaviour of the SCB specimens were determined by DIC analysis.

2. Materials and testing design
Raw materials
The investigation adopted raw materials consisting of gold mineralized zones collected in Mollehuaca, Arequipa, Peru. Geotechnical laboratory experiments were performed to determine the parameters of the MTs, including specific gravity, grain size distribution (GSD), and Atterberg limit. The testing were completed in accordance with ASTM standards D6913, D7928, and D4318. The geotechnical tests revealed a mean particle size of 76 μm with 49.9% tiny particles (<sieve #200). The coefficient of uniformity was determined as $Cu = 32.33$, with low plasticity (PI = 9.76%), a low liquid limit (LL = 22.80%), and low soil activity (A = 0.196). The compaction tests, meantime
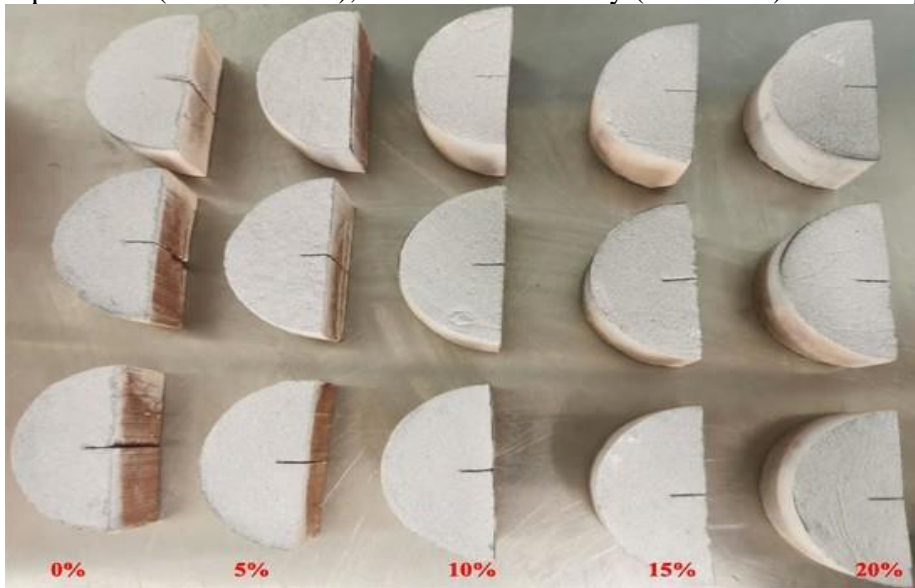

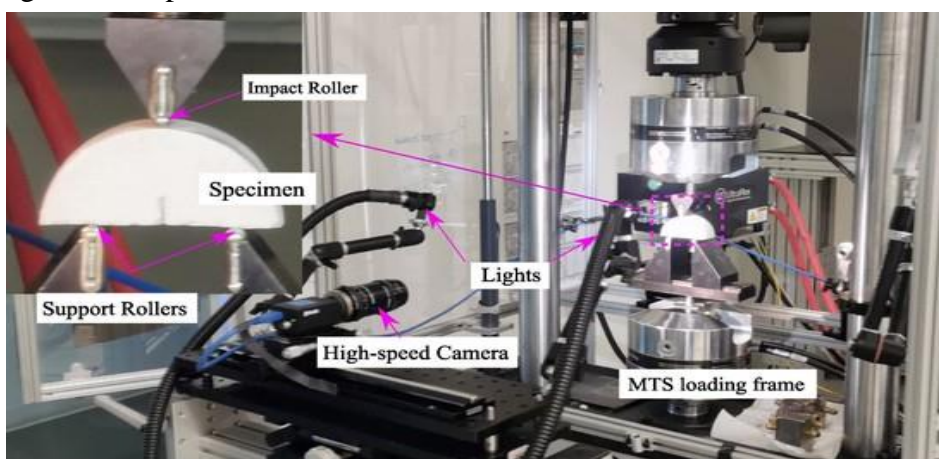Fig. 7. SCB specimens with different FA additions.

Fig. 8. Experimental setup of the SCB/NSCB tests of geopolymer.

Experiments were carried out utilising a Harvard small compaction mould to determine the optimal moisture content of 15.4%. Figure 1 displays a table containing the geotechnical parameters of the MTs. The MTs have particles that are 49.86% smaller than those retained on a #200 sieve. They are classed as Gravelly Lean Clay with Sand (CL) according to AASHTO classification as per ASTM D3282.

Class F fly ash (FA) was used in this work as an amorphous additive material to enhance reactivity and modify the Si: Al ratio. The mineral components of the MTs and FA were identified using X-ray diffraction (XRD) examinations utilising an X-ray diffractometer (Axios Omnian, PAN alytics B.V., Eindhoven, Netherlands) in the research. The reflection patterns were compared to the database to identify and quantify the crystal phases. Figure 2a displays the X-ray diffraction (XRD) analysis findings of the MTs and class F FA, revealing crystalline phases of quartz (Q), muscovite (M), and calcite (C) in the MTs, with quartz being the predominant mineral at 77.7%. Fig. 2b displays the XRD pattern of class F FA particles, revealing a reflection pattern at $2\theta = 15$-$35°$ that suggests a notable presence of amorphous aluminosilicates, which are highly reactive with alkaline solutions.
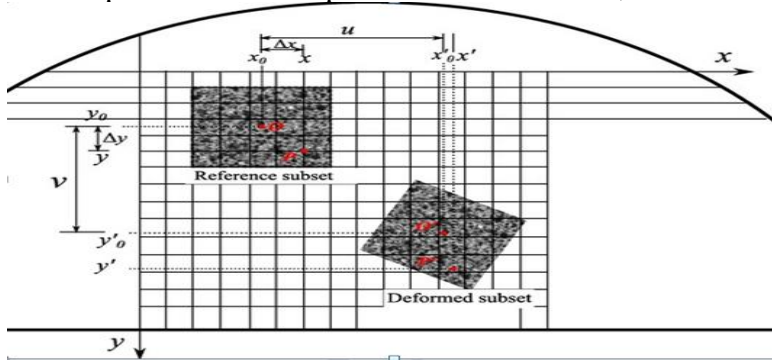

Fig. 9. Schematic diagram of digital image correlation.

Table 1 Geometric properties of all the SCB/NSCB specimens.

a/R	#1	0.29	0.28	0.29	0.31	0.28
	#2	0.29	0.29	0.29	0.25	0.30
	#3	0.31	0.29	0.27	0.31	0.30
D(mm)	#1	77.2	77.4	78.0	77.7	77.2
	#2	78.0	77.2	77.7	77.4	76.9
	#3	77.2	77.4	77.4	78.0	75.8
$2S$(mm)	#1	46.3	46.5	46.8	46.6	46.3
	#2	46.8	46.3	46.6	46.5	46.1
	#3	46.3	46.5	46.5	46.8	45.5
T(mm)	#1	36.5	36.2	36.1	36.1	36.6
	#2	36.2	36.2	35.8	37.0	36.7
	#3	35.4	35.9	36.2	36.8	36.4

The research used gold MTs in half as the primary raw materials and incorporated FA as the amorphous source to enhance geopolymerization. Before adding the alkaline activator, the powdery MTs and FA were combined to achieve even distribution of both components. Figure 3 displays the SEM micrographs of the raw components and combinations with various FA additions. Figure 3a displays a micrograph of untreated gold microtubules where the particles are freely arranged without any cementation. Spherical fatty acid particles of different sizes may be seen in Figure 3b. Figures 3c-3f show mixes with formic acid additions of 5%, 10%, 15%, and 20%, respectively.

Figure 4 displays the SEM/EDS analysis of MTs and FA to highlight the variations in their chemical compositions. The EDS analysis was performed by choosing the MTs particle and FA particle in a specified field. Figures 4a and 4b show the EDS spectra of MTs particle and FA particle, respectively. The results indicate that the intensity of aluminium in MTs particles is lower than in FA particles. However, Class F FA contains less calcium compared to MTs. Thus, in addition to modifying amorphous aluminosilicates to enhance geopolymerization as seen in Fig. 2, the Si: Al ratio may be altered by combining MTs and FA, resulting in changes to the cell architectures.

Constructing geopolymer materials with MTs

Figure 6 illustrates the steps for creating MTs-based geopolymer specimens. The activator used was an alkaline solution prepared by combining NaOH pellets (97%, Sigma-Aldrich) with water to achieve a molarity of 10 M. The NaOH solutions were left in the room for 15 minutes after mixing to dissipate heat. The raw materials (MTs and FA) were combined with various matrix (e.g., none, five percent, ten percent, fifteen percent, twenty percent FA by weight of total) for 10 minutes to evenly disperse FA particles for alkaline activation. The NaOH solution was combined with the raw mixes for 15 minutes and then covered with plastic wrappings to avoid water evaporation for 10 minutes in the room. The mixtures were compressed into cylindrical moulds using the same compacting method as described in prior research [6].
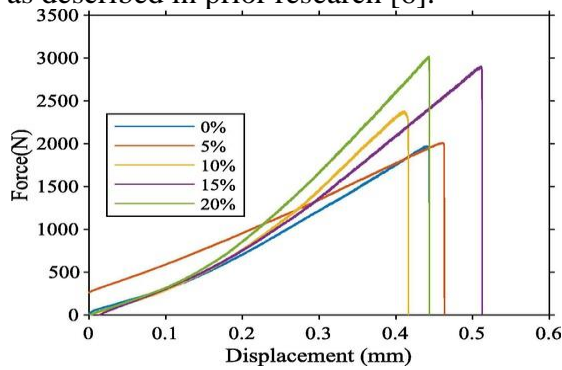

Fig. 10. Force-displacement relationship of the SCB specimen with different FA additions.
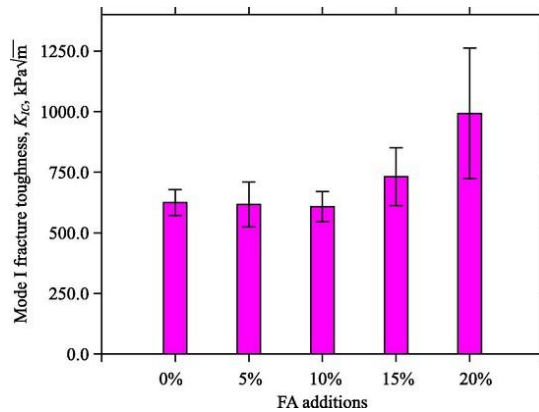

Fig. 11. Mode I fracture toughness of the geopolymer with different FA additions.

Table 2 Peak force and KIC value of the SCB specimens with different FA additions.

		0%	5%	10%	15%	20%
F_p (N)	#1	1914.40	2319.50	1955.00	2885.60	4312.80
	#2	1970.80	1724.50	2379.40	2125.96	3011.30
	#3	2087.70	2010.10	1725.80	2125.86	2406.00
	Mean Std.	1990.97	2018.03	2020.07	2379.14	3243.37
K_{IC} (kPa m$^{1/2}$)	#1	72.17	242.97	270.77	358.12	795.56
		580.33	719.25	624.92	869.51	1287.69
	#2	609.44	540.20	659.94	660.99	930.37
	#3	684.83	592.12	540.19	665.28	759.99
	Mean	624.87	617.19	608.35	731.93	992.68
	Std.	53.93	92.12	61.57	119.17	269.31

The cylindrical samples were removed from the moulds immediately after compaction and placed in an oven at 40 ± 2 °C for 24 hours. The SCB specimens were then put in an oven at a temperature of

70 ± 2 °C for an extra 6 days to cure. The step-by-step temperature control was implemented to prevent the rapid water evaporation at the beginning of the curing process in the oven, which might hinder the chemical reaction and integration of the specimen. Next, the treated samples will be examined using an MTS loading frame. The SCB tests were conducted as shown in Figure 5. Three SCB specimens were evaluated for geopolymer with the addition of each FA. Displacement-control loading mode at a rate of 0.05 mm/min was used for all experiments [38].
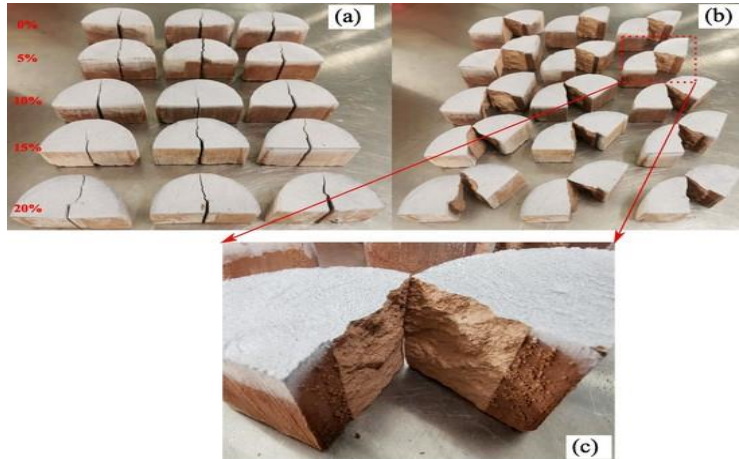

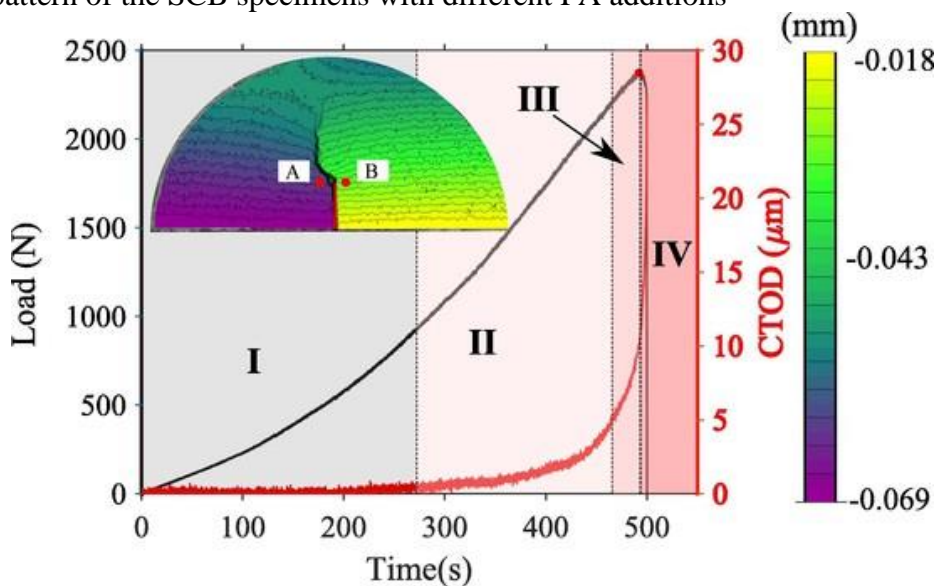Fig. 12. Failure pattern of the SCB specimens with different FA additions

Fig. 13. Crack propagation of the SCB specimen (FA = 10%) with different stages: I) elastic stage, II) fracture process zone, III) crack initiation, and IV) crack propaga- tion of post-peak crack evolution.

Semi-circular bending tests

The semi-circular bending tests were conducted in accordance with the ASTM D8044 standard. Figure 6 displays the schematic of the NSCB specimen. The NSCB specimens tended to break under loading due to two supporting rollers positioned at a same distance to the notch as the impact roller in the notch direction. The NSCB failed to withstand the yield caused by the tensile stress perpendicular to the fracture plane (mode I). Figure 7 displays the notched semi-circular bending specimens, while Figure 8 illustrates the experimental setup for the SCB/NSCB testing of geopolymer.
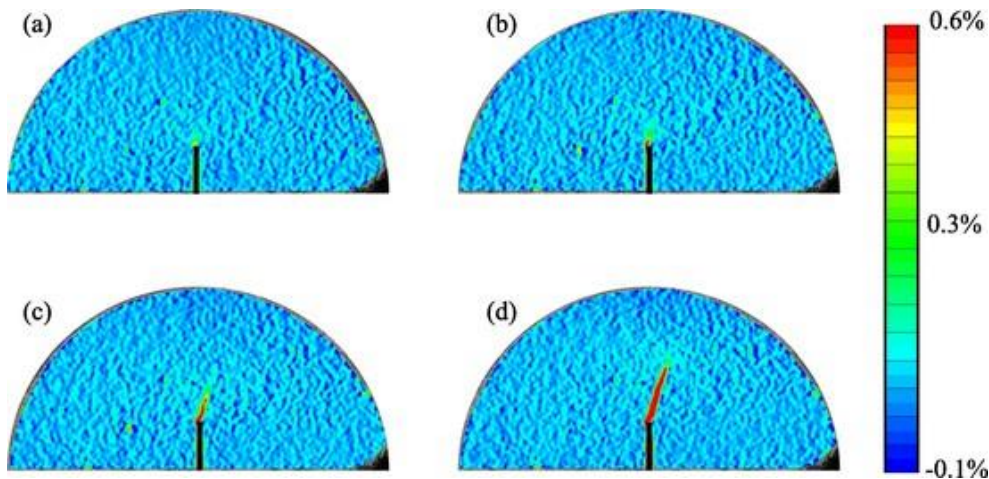
Fig. 14. Evolution of horizontal strain at different stages: a) stage I, b) stage II, c) stage III, and d) stage IV (0% FA addition).

Three relative notch depths, pre-designed as a/R = 0.3, were created using a hacksaw. Nevertheless, the actual dimensions of the SCB specimens, as shown in Table 1, were obtained using DIC. Three identical specimens were produced with the same notch depth replicated three times. The actual relative notch depths varied from 0.25 to 0.31, with an average of 0.29. were quantified using the pictures ac-

3. Synchronisation of digital images
The essentials of the development of DIC
DIC represents an experimental method that is non-destructive and may be used to measure macroscopic parameters like strain and displacement in brittle materials (e.g., rocks, concrete) by analysing pictures taken before and after deformation.2D Digital Image Correlation (DIC) is often used to quantitatively evaluate flat surfaces, especially for studying brittle materials. The specimen surfaces were prepared for picture collection by spray painting black dots on a white background. The black dots needed to be tiny to achieve precise correlation. The picture sequences are then recorded using a high-speed camera during the loading process. Surface deformations may be determined by comparing the pixel brightness of photographs taken before and after loading.

The DIC analyses were implemented using a reference picture supplied as the starting image of the image series [54,57]. Selected photographs of distinct loading circumstances were connected with a reference image to determine the deformation and macroscopic parameters of the specimen using a flat surface. The chosen photos were separated into subsets during image correlation based on the gray-scale intensity values of a particular number of pixels. Hence, the displacements and stresses may be determined by observing the deformations of each associated subset [56]. The paper utilised Vic-2D DIC software to post-process and extract the full-field displacements/strains of the specimen surfaces. Input parameters, such as subset size (15 pixels) and step size (5 pixels), were chosen based on values from previous literature [52,57]. Hence, the distortions of the geopolymer SCB specimens under constant stress may be monitored using picture capture. Figure 9's correlation diagram illustrates the deformation of a subset before and after deformation. The relative translational deformation of the subset centre can be monitored by measuring the displacement of O(O') and the rational deformation relation can be monitored by measuring the displacements of P(P'). The correlation principle can be expressed as follows:

$$x' = x_0 + \Delta x + u + \frac{\partial u}{\partial x}\Delta x + \frac{\partial u}{\partial y}\Delta y$$
$$y' = y_0 + \Delta y + v + \frac{\partial v}{\partial x}\Delta x + \frac{\partial v}{\partial y}\Delta y \qquad (1)$$

3.2 Strain acquisition from DIC

MTs-based geopolymer, like rock samples, exhibits varied impacts on mechanical, fracture, and strain characteristics under loadings, which were usually analysed using DIC. Various scholars extensively studied the impact of small-scale variations on the multi-scale behaviours of brittle materials using numerical simulations utilising the discrete element approach. Various direct and indirect procedures were described in the laboratory. These included X-ray computerised tomography and thin-section examination using scanning electron microscopy. Geopolymers based on metakaolin offer great potential for use in manufacturing construction materials. Therefore, a thorough knowledge of their strain behaviour is essential. Furthermore, the methods discussed mostly focused on analysing materials of high strength, such as granites and sandstone. The geopolymer based on MTs is a brittle material with a restricted compression strength of around 30 MPa as described by [39].
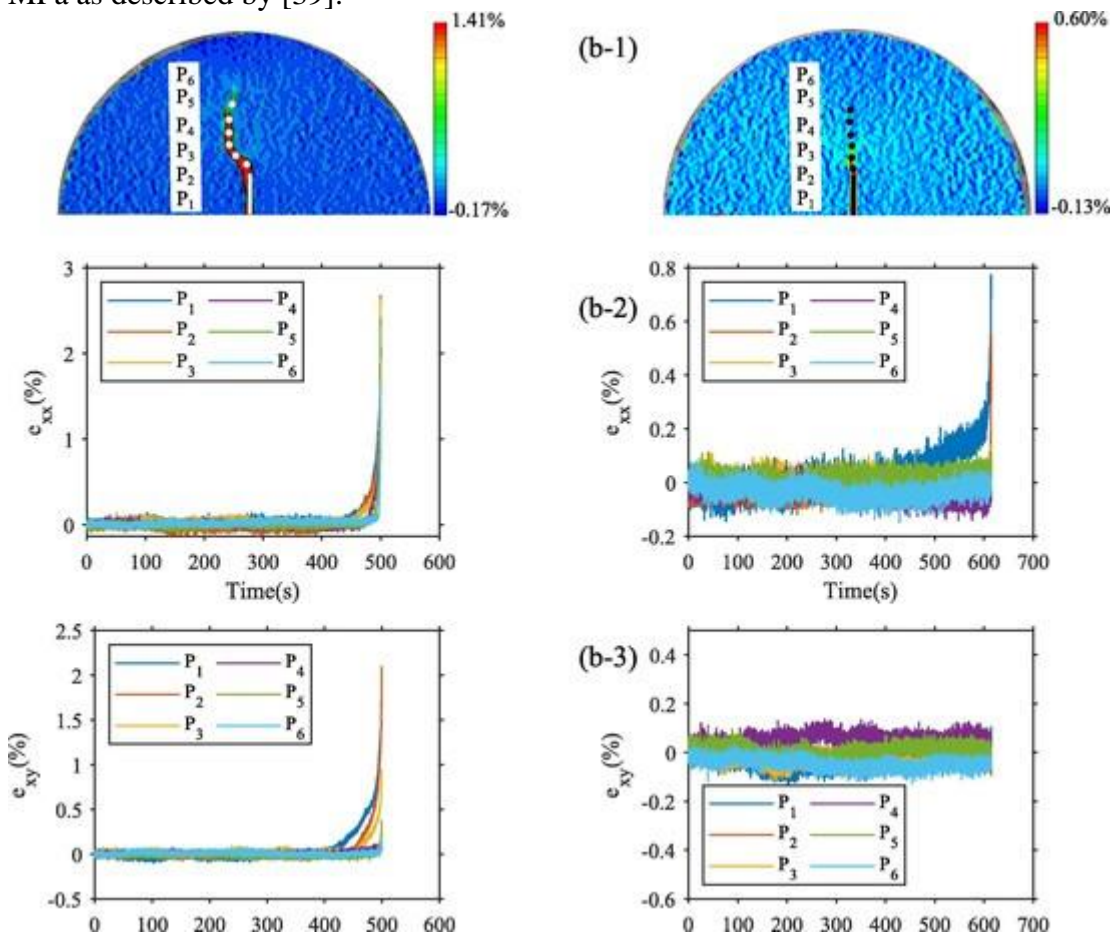
Fig. 15. Normal strain and shear strain evolution with time for the SCB specimens with a) 10% and b) 15% FA additions, a-2 and b-2 are the evolution of normal strains and a-3 and b-3 are the evolution of shear strains.

This approach may readily disrupt the geo-polymeric cell structure and is thus rather unsuitable. The article highlights the tremendous potential of 2D DIC in studying the strain behaviors' of geo-polymer. Several studies extensively documented the strain behaviors' of brittle materials using DIC, such as in references [63,64]. The Green-Lagrange strains may be determined accordingly.

4. Results and discussion

Force-displacement relationship

The following section presents the force-displacement curves of geopolymer SCB specimens with varied FA additions to assess their impact on strength resistance behaviours. Figure 10 displays the development of force over time for the chosen SCB specimens with varying notch depths. Under the present loading circumstances, the forces gradually develop and then follow a linear pattern until failure, which is indicated by an abrupt reduction in force. The first adjustment somewhat raised the recommended specimen parameters. The bottom surfaces and top margins of the SCB specimens may not be parallel.
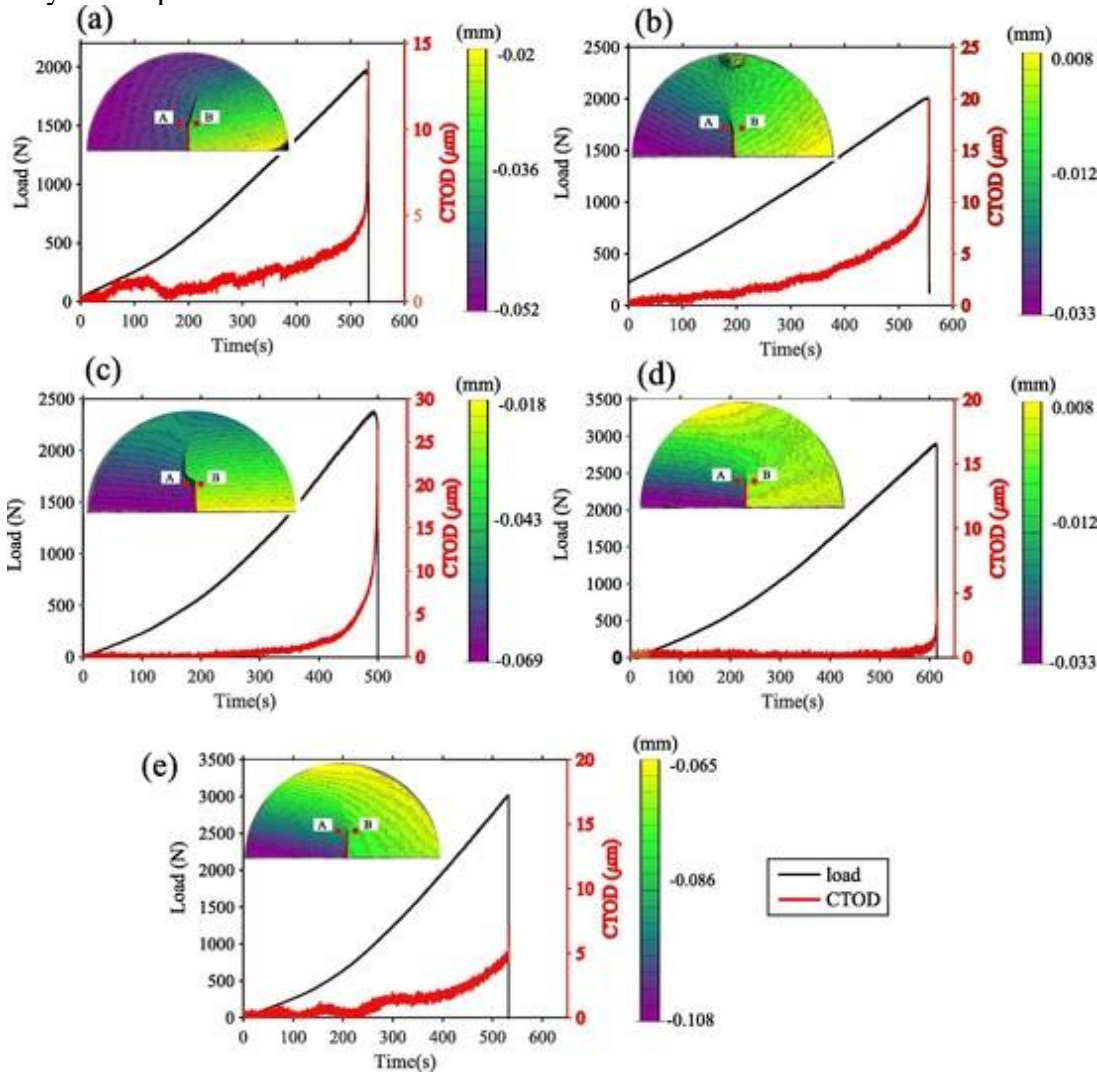
Fig. 16. Evolution of force and crack tip opening displacement as a function of time, a)-e) correspond to 0, 5%, 10%, 15%, and 20% percentage of FA addition.

Once the force reached about 300 N, the force-displacement curve showed a linear rise. When a setting force of 300 N was applied, the force-displacement curve exhibited a linear pattern for the SCB specimen with 5% FA addition, as seen in Fig. 10. Findings indicate that increasing the FA adds results in a proportional increase in the maximum force achieved. The highest resistance levels indicated the strengths of the geopolymer specimens, with the geopolymer while 15% FA additions exhibiting the greatest strength.

Mode I fracture toughness

Tailings-based geopolymer exhibits qualities similar to cement mortars, but with bigger particle sizes that undergo varying levels of alkali-activation. Fractures may be categorised into three categories based on the sort of stress applied: opening mode (mode I), shearing mode (mode II), and tearing mode (mode III). NSCB specimens with the same distance from supporting rollers to the notch and the impact roller in alignment with the notch experienced mode I fracture (opening). The Linear Elastic Fracture Mechanics (LEFM) approach was often used to calculate the mode I fracture toughness as per the equation provided by Kuruppu [65]. Applying Linear Elastic Fracture Mechanics (LEFM) to estimate the mode I fracture toughness may be influenced by the size impact caused by inelasticity at notch tips or the fracture process zone. However, it may still be used for estimating purposes based on the specimen sizes in this research. Many researchers extensively used the LEFM assumption to assess fracture toughness in brittle materials, as shown by many studies (e.g., [21, 68–76]). The mode I stress intensity factor of the geopolymer specimens at current sizes was determined using calculations based on the Linear Elastic Fracture Mechanics (LEFM) for the NSCB specimens. If the NSCB specimens experienced linear elastic fracture before cracking start, the mode I stress intensity factor may be estimated as follows:
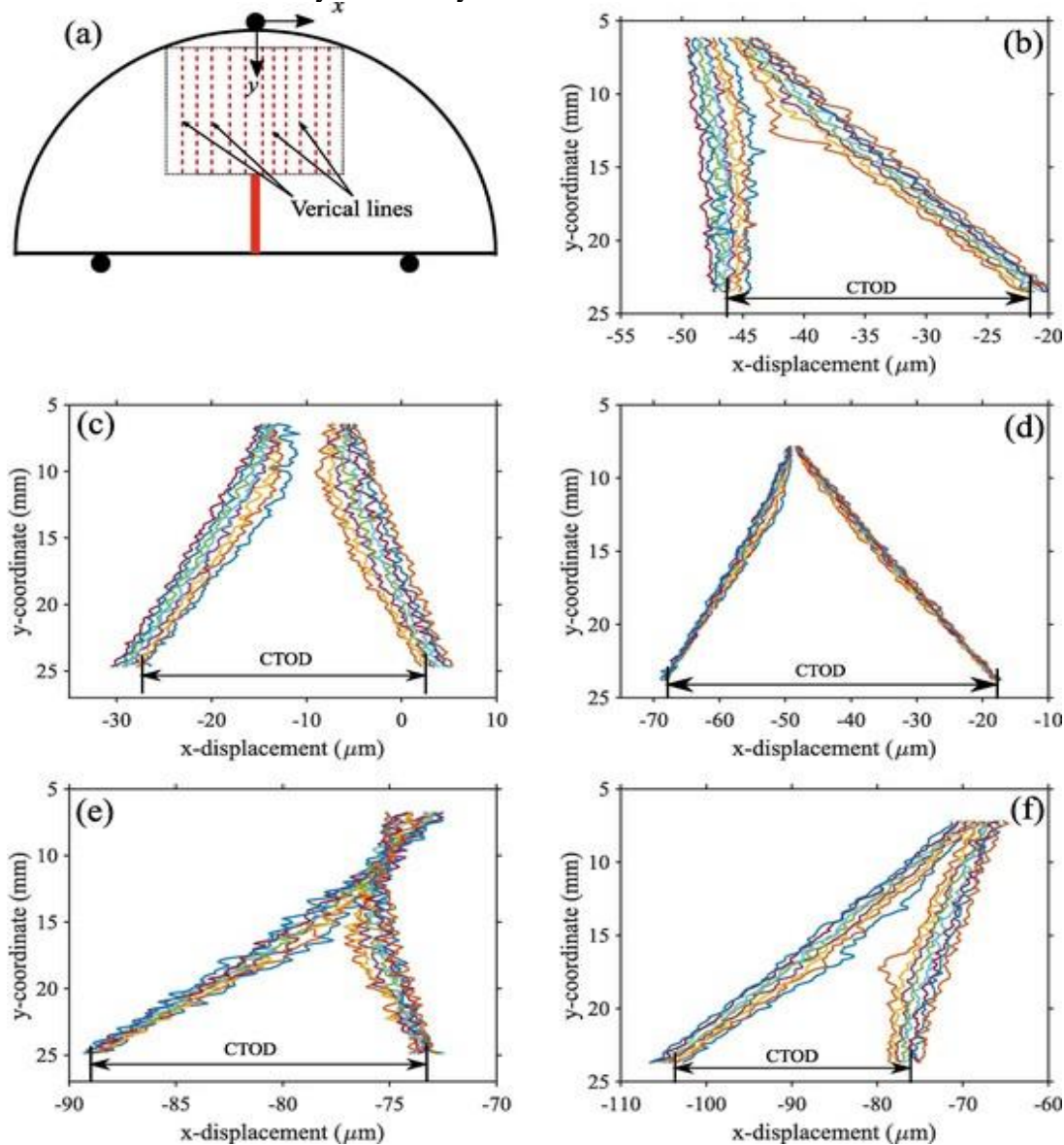
Fig. 17. Diagram of CTOD at peak load for the SCB specimens with different FA additions: a) diagram of selected vertical virtual lines, b) without FA addition, c) 5% FA additions, d) 10% FA additions, e) 15% FA additions, and e) 20% FA additions

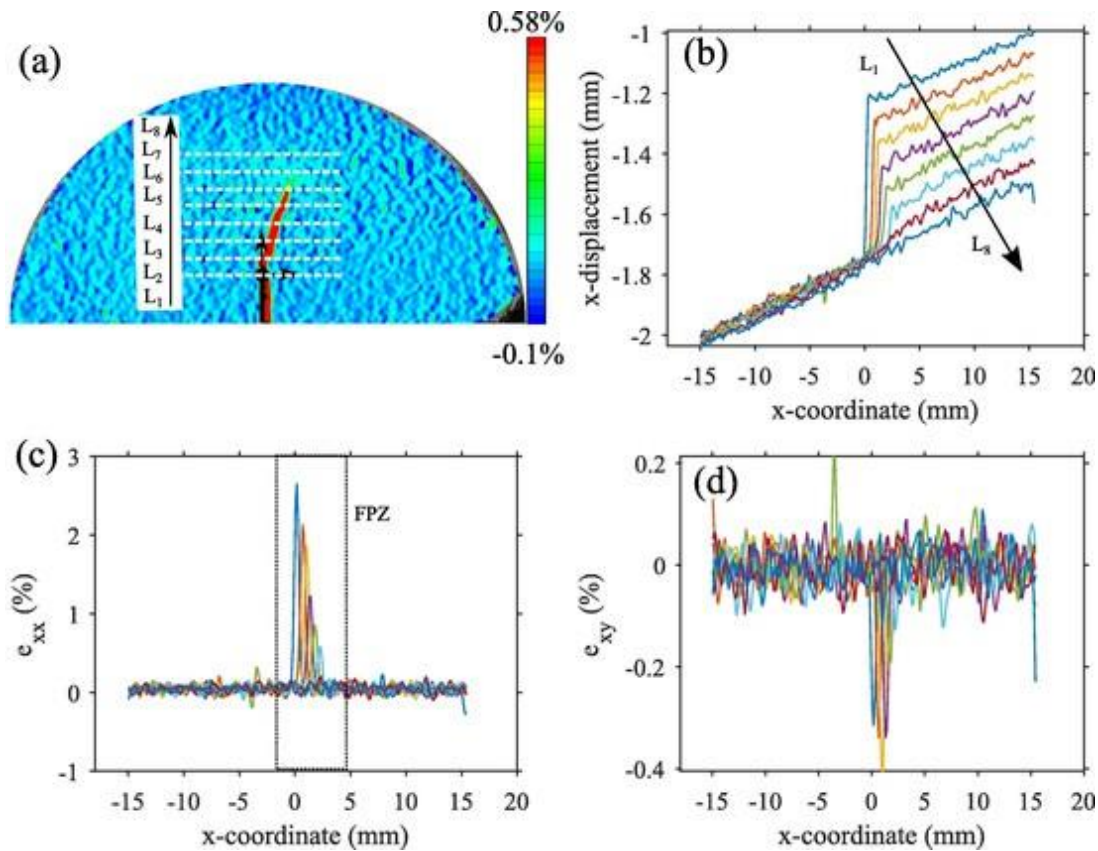$$K_I = \frac{F\sqrt{\pi a}}{2RT} Y_I \qquad \textbf{(5)}$$

Figure 18 illustrates the description of FPZ for the SCB specimen without FA additions. It includes a graphic of chosen horizontal virtual lines, x-displacements at the virtual lines, εxx on the virtual lines, and εxy on the virtual lines.

YI is an arbitrary factor which quantifies the crack-tip strain magnitude, which is described as a geometric parameter associated with the notch and span features [44,65,66]. The stress intensity factor at peak, KIC, is a measure of fracture toughness. The mode I fracture toughness may be determined by entering the maximum loads into the equations. Items 5 and 6. Table 2 lists the peak forces and critical stress intensity factor, KIC, of the SCB specimens with various FA additions. The average peak forces for the SCB specimens ranged from 1990.97 N to 3243.37 N, showing significant variations, for SCB specimens with and without 5–20% FA increases. The peak force averaged for the SCB specimens was smallest when no FA was added, while it was biggest for the SCB specimen with 20% FA. The peak forces without adding FA and with 5% and 10% were of equal magnitudes. The mode I critical stress intensity factor or fracture toughness, KIC, was computed by putting the forces and geometric parameters of the SCB specimens into equations (5) and (6). The results are shown in Table 2 and Fig. 11. The KIC value of the SCB varied between 608.35 and 992.68 kPa•m0.5 according to the results. Under the present curing conditions, adding a limited amount of FA (e.g., 5% and 10%) did not affect the mode I fracture toughness of the geopolymer when compared to the geopolymer without FA addition [54]. FA addition had varying effects on the enhancement of mode I fracture toughness compared to its effects on uniaxial compression and splitting tensile strengths, as shown by Zhang et al. [6,78].

Minor amounts of FA have minimal impact on the geopolymer's resistance to fracture propagation. Significant increases in the KIC values were seen in the SCB specimen with 15% and 20% FA additions.

Failure pattern

The distances between two supporting rollers and the notch of the notched SCB specimen were the same, as shown in Fig. 6. The notched SCB specimens were tested in pure mode I conditions, causing the open fractures in the specimens to appear in response to the stress. The notch tips experienced pure tensile failure, causing open fractures to propagate from the notch tips to the impact roller as seen in Figure 6. Figure 12a displays fractured specimens with and without various FA additions, revealing noticeable penetrating fractures extending from notch tips to the impact roller. Because of the material heterogeneity, the crack propagation patterns varied across all the specimens, displaying curved fracture patterns. Figure 12b illustrates that all the SCB specimens had convoluted failure surfaces as a result of their varied behaviours. Figure 12c displayed a detailed view of the fractured surface, revealing intricate surface curvatures.
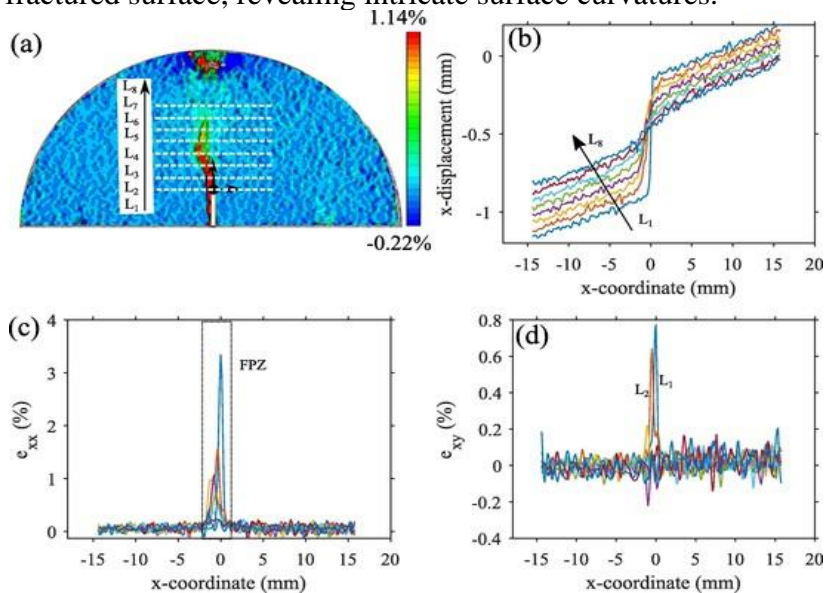

Figure 19 demonstrates the FPZ identification for the SCB specimen with 5% FA additions. a) schematic of certain horizontal imaginary lines, b) x-displacements at the imaginary lines, c) εxx on the imaginary lines, and d) εxy on the imaginary lines.

Crack evolution of the SCB specimen

MTs-based geopolymer is a brittle material with rapid brittle points and fracture propagation that are not easily observable. DIC was used as a nondestructive approach to analyse the initiation, phases, and development of the geopolymer SCB samples. Crack propagation characteristics of SCB specimens with varying FA additions may be assessed by monitoring crack tip opening displacements (CTOD) over time. Figure 13 displays the load-time and CTOD-time evolution of the chosen SCB specimen. Figure 13 displays an inset figure illustrating the x-displacement contour map and the points of interest (POI) used to determine the x-displacements necessary for CTOD calculations. Points A and B are equidistant horizontally from the notch tip on opposite sides. The x-coordinates of points A and B changed as they were loaded, and the CTOD was determined by computing the differences in x-coordinates of the chosen points of interest (A, B). The CTOD-time and load-time connections are presented in the same figure to identify the fracture development phases of the chosen SCB specimen more effectively. The crack development phases may be identified based on the CTOD progression of the chosen SCB specimens acquired from the POIs. Four distinct phases were identified via the recognition of CTOD

development. Results indicate that the CTOD remained stable at zero until 277.5 seconds, after which it began to steadily rise. The CTOD rose in a convex manner till reaching 474.6 seconds. The CTOD exhibited exponential growth from 474.6 s to 494.1 s, followed by a dramatic spike at the conclusion of the testing. Between 0 s and 277.5 s, the stage was characterised by elastic behaviour and specimen setting (I), with no noticeable CTOD seen. This was followed by a fracture process zone (II) from 277.5 s to 474.6 s, leading to crack initiation at 494.1 s. The SCB specimen attained its maximum load after 494.1 seconds. Stage III began at 474.6 s with fracture commencement and ended at 494.1 s with the peak load, signalling the onset of crack propagation and post-peak crack development in Stage IV. The sudden increase at stage IV indicated the progression of the fracture till the specimen failed.

Fracture behavior obtained from DIC
Strain behavior of the geopolymer
The strain values of the Single-Cantilever Beam (SCB) specimens were determined using equations (2–4). For Green-Lagrange strain, a positive number indicates tensile stress while a negative value indicates compression. The SCB began cracking due to tensile stress at the notch points under mode I loading. Fig. 14 displays the horizontal strain contour maps of the chosen SCB specimen without FA addition at various phases as specified in Fig. 13. The development of horizontal strain at notch tips clearly showed that tensile strain was spreading in the SCB specimen at the notch. The horizontal strain at stage I was evenly spread out as seen in Fig. 14(a). In stage II of the fracture process, there was a minor concentration of strain at the notch tip, as seen in Fig. 14(b). Cracks began to form and spread throughout stage III, leading to increased strain concentrations as seen in Figure 14(c). A distinct fracture pattern was found in stage IV due to the concentrated horizontal strain, as seen in Fig. 14(d). The horizontal strain map indicated that tensile stresses were only present at the notch tips, where the Single-Cantilever Beam (SCB) experienced tensile stress under mode I loading.
Six monitoring sites, P1 through P6, were chosen on the strain concentration areas of SCB specimens with various FA additions to observe the development of horizontal strains over time, as seen in Fig. 15 (a-1 and b-1). P1 represented the notch tip and P6 was the furthest point from the notch tips, as illustrated in Fig. 15. The contour maps in Fig. 15 (a-1 and b-1) display the chosen monitoring points. The middle row depicts the progression of horizontal strains, εxx, over time, while the bottom row shows the development of shear strain, εxy, in the selected SCB specimens. Thus, evaluating the horizontal and shear stresses over time may provide insights into the development of strain behaviours and fracture types in SCB specimens. Horizontal and normal stresses were used to show fracture opening, whereas shear strains were used to detect the presence of shear cracks.
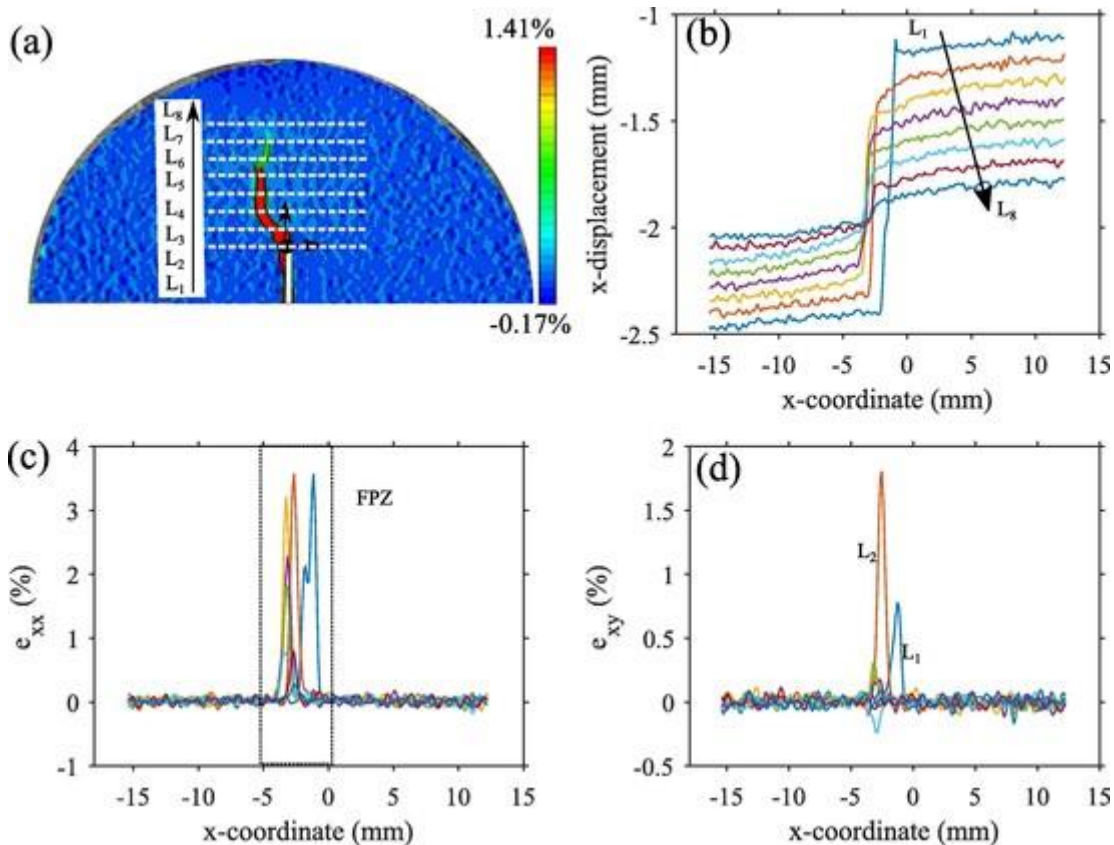
Fig. 20. FPZ identification for the SCB specimen with 10% FA additions: a) diagram of selected horizontal virtual lines, b) x-displacements at the virtual lines, c) εxx on the virtual lines, and d) εxy on the virtual lines.

During the alkali activation process, the particles of tailing soils underwent partial reaction and dissolution. Grain heterogeneity persisted in the specimens even after being exposed to mode I loading conditions. Stress variations lead to strain variations, disturbances, and the spread of fractures in the tailings-based geopolymer. The addition of 10% FA led to the development of shear strain and a complex fracture surface in the SCB specimens, particularly evident in Fig. 15(a-3) where strain began to grow at 400 s. While strain contour maps may be used to analyse the general failure pattern of geopolymer specimens, they are not effective in identifying the kinds of cracks. Hence, monitoring the development of both normal and shear stresses was necessary to identify the possibility of shear fractures. Fig. 15 shows the progression of shear strain together with normal stresses. The strain evolution was affected by noise due to the mathematical method used to derive displacement. Yet, the stresses during the elastic or specimen-setting phases may also provide precise assessments of evolutionary characteristics. While theoretical solutions may be used to calculate strain, many researchers regularly watch the strain history of Points of Interest (POIs) on fracture surfaces to examine the strain behaviour of brittle materials like rocks and concretes. The normal and shear stresses of the SCB specimens with 10% and 15% FA additions showed fracture phases that aligned with the development of horizontal strains over time, consistent with the CTOD progression seen in Fig. 13. Furthermore, the horizontal strain development showed that the horizontal strain rose sooner the closer the chosen point was to the notch tip. Figure 15 shows two SCB specimens with differing failure patterns: the SCB with 10% FA addition has a curved fracture surface, while the one with 15% FA addition has a rather straight surface. The analysis of shear stresses indicated that, in addition to the tensile fracture, the SCB specimen containing 10% FA also experienced shear cracking.
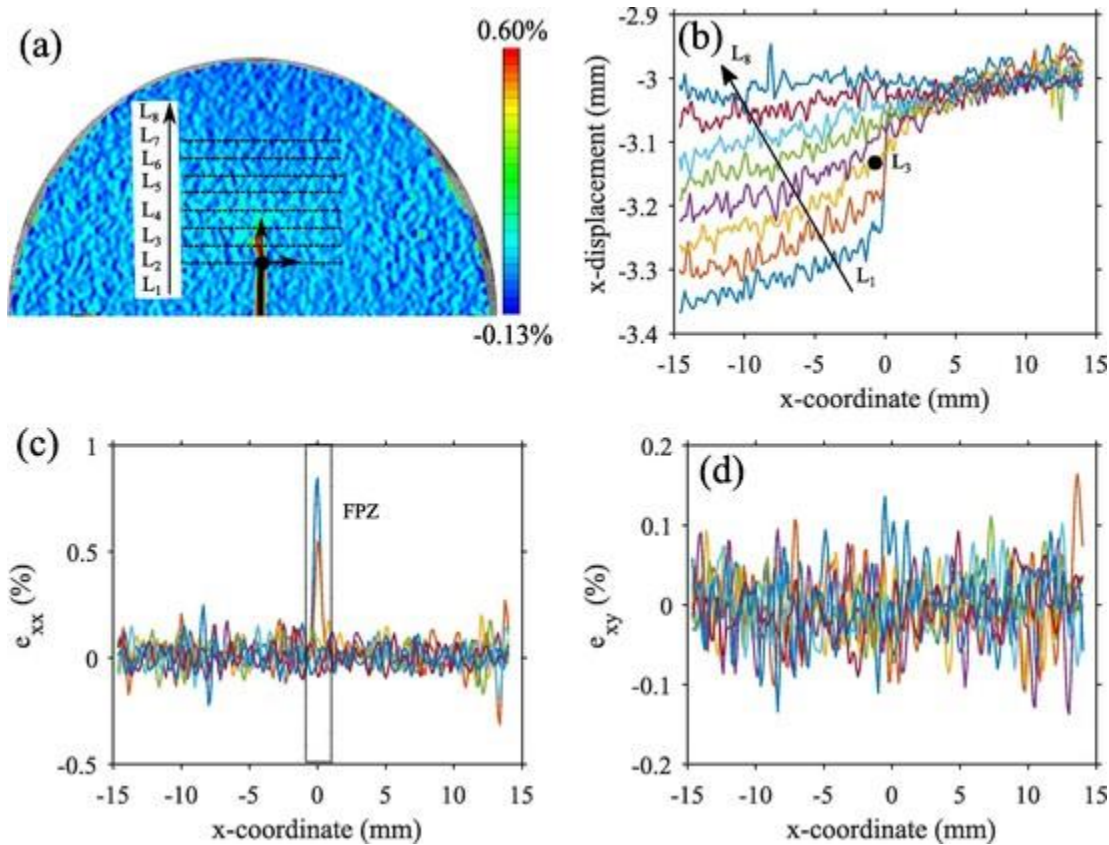
Figure 21 displays the FPZ identification for the SCB specimen with 15% FA additions. a) schematic of specific horizontal imaginary lines, b) x-shifts at the imaginary lines, c) normal strain in the x-direction on the imaginary lines, and d) shear strain on the imaginary lines.

The shear strain development of P1, P2, and P3 indicated that the shear strains began to appear at the crack onset, as shown in Fig. 13. Shear cracks under mode I conditions may be caused by material heterogeneity, specimen setup, and changes in notch directions. Thus, mixed-mode cracking occurred. Shear strain evolution in SCB specimens with 15% clearly showed little presence of shear fractures. Under mode I loading conditions, the SCB specimen exhibited both tensile and shear fractures with a convoluted fracture surface, whereas the SCB specimens with a straight cracked surface only showed pure tensile cracks.

5. Conclusions

Everyone inserted Class F fly ash as a nebulous part to the gold MTs-based geopolymer to make it stronger and less likely to break. This research used gold MTs with 5%, 10%, 15%, and 20% FA, mixed with NaOH solution at a lower liquid-to-solid ratio of 16%, pressed down with an HMC tamper, and hardened at a high temperature to create an MTs-based geopolymer structure. We then looked into how the mode I fraction behaved by running a series of SCB tests with mode I loading conditions. At the same time, 2D DIC was used to find out how the SCB specimens with different amounts of FA behaved under force and when they broke. We are taking back the main conclusions because

a.   Using the given cure conditions and liquid-to-solid ratio, the forces on the SCB samples under mode I loading went up slightly at first, then steadily rose until they broke, as shown by the sudden drops in force. It looks like adding smaller amounts of FA doesn't have much of an effect on the mode I fracture toughness (KIC); however, adding 15% and 20% FA made KIC go up. The biggest KIC was at 20% FA increase.

b.   When loaded in mode I, all of the SCB samples had an entry fracture pattern that went from

the tip of the notch to the impact roller. But because the materials were not all the same and the way the experiment was set up, the crack spread patterns of each object were different, and bent fracture patterns were seen.

c.   Scientists used DIC to figure out how cracks in the SCB formed by watching how CTOD changed over time. The cracks in the notched SCB samples went through a total of four phases: the elastic stage, the FPZ stage, the crack onset stage, and the post-peak crack spread stage. The SCB samples' horizontal strains at different stages showed that the strain concentration began at the FPZ stage at the notch tips and then spread to the effect on the blade.

d.   Applying a setting force when loading made the CTOD-identified elastic stage less apparent. Besides that, there were four levels to the CTOD. Averaging the x-displacement differences of the chosen vertical lines from the DIC allowed us to estimate the CTOD of the SCB specimens. We measured the lengths of the FPZ by using the x-displacement in the specified virtual horizontal lines. The duration of the FPZ is often shorter as the proportion of FA addition is larger. The alterations in horizontal strain on the lines also indicated the FPZ lengths.

References

[1]   Tho-In T, Sata V, Boonserm K, Chindaprasirt P. Compressive strength and microstructure analysis of geopolymer paste using waste glass powder and fly ash. J Cleaner Prod 2018;172:2892–8.

[2]   Falayi T, Ntuli F, Okonta F. Synthesis of a paste backfill geopolymer using pure acidic gold mine tailings. J Solid Waste Technol Manage 2018;44(4):311–20.

[3]   Falayi T. A comparison between fly ash-and basic oxygen furnace slag-modified gold mine tailings geopolymers. Int J Energy Environ Eng 2019;1–11.

[4]   Zhang N, Hedayat A, Bolaños H.G, González J.J, Salas G.E, Ascuña V.B. Damage evaluation and deformation behavior of mine tailing-based geopolymer under uniaxial cyclic compression. Ceram Int 2021;47(8):10773–85.

[5]   Zhang N, Hedayat A, Bolaños Sosa H.G, González Cárdenas J.J, Salas Álvarez G.E, Ascuña Rivera V.B. Specimen size effects on the mechanical behaviors and failure patterns of the mine tailings-based geopolymer under uniaxial compression. Constr Build Mater 2021;281:122525.

[6]   Zhang N, Hedayat A, Sosa H.G.B, Tupa N, Morales I.Y, Loza R.S.C. Crack evolution in the Brazilian disks of the mine tailings-based geopolymers measured from digital image correlations: An experimental investigation considering the effects of class F fly ash additions. Ceram Int 2021;47(22):32382–96.

[7]   Singh B, Ishwarya G, Gupta M, Bhattacharyya S.K. Geopolymer: A review of some recent developments. Constr Build Mater 2015;85:78–90.

[8]   Davidovits J. Geopolymers: Chemistry and Applications. Geopolymer institute; 2020.

[9]   Rattanasak U, Chindaprasirt P. Influence of NaOH solution on the synthesis of fly ash geopolymer. Miner Engng 2009;22(12):1073–8.

[10]   Olivia M, Nikraz H. Properties of fly ash geopolymer designed by Taguchi method. Mater Des 2012;1980–2015(36):191–8.

[11]   Alanazi H, Yang M, Zhang D, Gao Z. Early strength and durability of metakaolin-based geopolymer. Mag Concr Res 2017;69(1):46–54.

[12]   Nath P, Sarker P.K. Flexural strength and elastic modulus of ambient-cured blended low-calcium fly ash geopolymer. Constr Build Mater 2017;130:22–31.

[13]   Mehta A, Siddique R, Ozbakkaloglu T, Uddin Ahmed Shaikh F, Belarbi R. Fly ash and ground granulated blast furnace slag-based alkali-activated concrete: Mechanical, transport and microstructural properties. Constr Build Mater 2020;257:119548.

[14] Albidah A, Altheeb A, Alrshoudi F, Abadel A, Abbas H, Al-Salloum Y. Bond performance of GFRP and steel rebars embedded in metakaolin based geopolymer. Structures 2020;27:1582–93.

[15] Albidah A, Alghannam M, Abbas H, Almusallam T, Al-Salloum Y. Characteristics of metakaolin-based geopolymer for different mix design parameters. J Mater Res Technol 2021;10:84–98.

[16] Praveen Kumar V.V, Prasad N, Dey S. Influence of metakaolin on strength and durability characteristics of ground granulated blast furnace slag based geopolymer. Structural Concrete 2020;21(3):1040–50.

[17] Ren B.o, Zhao Y, Bai H, Kang S, Zhang T, Song S. Eco-friendly geopolymer prepared from solid wastes: A critical review. Chemosphere 2021;267:128900.

[18] Zhao J, Tong L, Li B, Chen T, Wang C, Yang G, et al. Eco-friendly geopolymer materials: A review of performance improvement, potential application and sustainability assessment. J Cleaner Prod 2021;307:127085.

[19] Kiventerä J, Lancellotti I, Catauro M, Dal Poggetto F, Leonelli C, Illikainen M. Alkali activation as new option for gold mine tailings inertization. J Cleaner Prod 2018;187:76–84.

[20] Zhang N, Hedayat A, Bolaños Sosa H.G, Tunnah J, González Cárdenas J.J, Salas Álvarez G.E. Estimation of the mode I fracture toughness and evaluations on the strain behaviors of the compacted mine tailings from full-field displacement fields via digital image correlation. Theor Appl Fract Mech 2021;114:103014.

[21] Zhang N, Hedayat A, Bolaños Sosa H.G, Tupa N, Yanqui Morales I, Canahua Loza R.S. Mechanical and fracture behaviors of compacted gold mine tailings by semi-circular bending tests and digital image correlation. Constr Build Mater 2021;306:124841.

[22] Ahmari S, Zhang L. Production of eco-friendly bricks from copper mine tailings through geopolymerization. Constr Build Mater 2012;29:323–31.

[23] Argane R, Benzaazoua M, Hakkou R, Bouamrane A. Reuse of base-metal tailings as aggregates for rendering mortars: Assessment of immobilization performances and environmental behavior. Constr Build Mater 2015;96:296–306.

[24] Zhao Y, Gong J, Zhao S. Experimental study on shrinkage of HPC containing fly ash and ground granulated blast-furnace slag. Constr Build Mater 2017;155: 145–53.

[25] Chindaprasirt P, Rattanasak U. Fire-resistant geopolymer bricks synthesized from high-calcium fly ash with outdoor heat exposure. Clean Technol Environ Policy 2018;20(5):1097–103.

[26] Zhang N, Hedayat A, Figueroa L, Steirer K.X, Li H, Bolaños Sosa H.G, et al. Experimental studies on the durability and leaching properties of alkali-activated tailings subjected to different environmental conditions. Cem Concr Compos 2022;130:104531.

[27] Jiao X, Zhang Y, Chen T. Thermal stability of a silica-rich vanadium tailing based geopolymer. Constr Build Mater 2013;38:43–7.

[28] Demir F, Derun E.M. Modelling and optimization of gold mine tailings based geopolymer by using response surface method and its application in Pb2+ removal. J Cleaner Prod 2019;237:117766.

[29] do Carmo e Silva Defáveri K, dos Santos L.F, Franco de Carvalho J.M, Peixoto R.A.F, Brigolini G.J. Iron ore tailing-based geopolymer containing glass wool residue: A study of mechanical and microstructural properties. Constr Build Mater 2019;220:375–85.

[30] Manjarrez L, Nikvar-Hassani A, Shadnia R, Zhang L. Experimental study of geopolymer binder synthesized with copper mine tailings and low-calcium copper slag. J Mater Civ Engng 2019;31(8):4019156.

[31] Moukannaa S, Nazari A, Bagheri A, Loutou M, Sanjayan J.G, Hakkou R. Alkaline fused

phosphate mine tailings for geopolymer mortar synthesis: Thermal stability, mechanical and microstructural properties. J Non-Cryst Solids 2019;511:76–85.

[32] Wang S, Xue Q, Zhu Y, Li G, Wu Z, Zhao K. Experimental study on material ratio and strength performance of geopolymer-improved soil. Constr Build Mater 2021;267:120469.

[33] Hu S, Zhong L, Yang X, Bai H, Ren B.o, Zhao Y, et al. Synthesis of rare earth tailing-based geopolymer for efficiently immobilizing heavy metals. Constr Build Mater 2020;254:119273.

[34] Tian X, Xu W, Song S, Rao F, Xia L. Effects of curing temperature on the compressive strength and microstructure of copper tailing-based geopolymers. Chemosphere 2020;253:126754.

[35] Nguyen K.T, Ahn N, Le T.A, Lee K. Theoretical and experimental study on mechanical properties and flexural strength of fly ash-geopolymer. Constr Build Mater 2016;106:65–77.

[36] Farina I, Modano M, Zuccaro G, Goodall R, Colangelo F. Improving flexural strength and toughness of geopolymer mortars through additively manufactured metallic rebars. Compos B Engng 2018;145:155–61.

[37] Ahmed H.Q, Jaf D.K, Yaseen S.A. Flexural strength and failure of geopolymer beams reinforced with carbon fibre-reinforced polymer bars. Constr Build Mater 2020;231:117185.

[38] Zhang N, Hedayat A, Bolaños Sosa H.G, Huamani Bernal R.P, Tupa N, Yanqui Morales I, et al. On the incorporation of class F fly-ash to enhance the geopolymerization effects and splitting tensile strength of the gold mine tailings-based geopolymer. Constr Build Mater 2021;308:125112.

[39] Zhang N, Hedayat A, Bolaños Sosa H.G, González Cárdenas J.J, Salas Álvarez G.E, Ascuña Rivera V, et al. Fracture and Failure Processes of Geopolymerized Mine Tailings under Uniaxial Compression. 54th US. Golden, CO, USA: Rock Mechanics/Geomechanics Symposium; 2020.

[40] Zhao S, Xia M, Yu L, Huang X, Jiao B, Li D. Optimization for the preparation of composite geopolymer using response surface methodology and its application in lead-zinc tailings solidification. Constr Build Mater 2021;266:120969.

[41] Mansouri H, Ajalloeian R. Mechanical behavior of salt rock under uniaxial compression and creep tests. Int J Rock Mech Min Sci 2018;110:19–27.

[42] Gong F, Yan J, Luo S, Li X. Investigation on the linear energy storage and dissipation laws of rock materials under uniaxial compression. Rock Mech Rock Engng 2019;52(11):4237–55.

[43] Nguyen T.T, Bui H.H, Ngo T.D, Nguyen G.D, Kreher M.U, Darve F. A micromechanical investigation for the effects of pore size and its distribution on geopolymer foam concrete under uniaxial compression. Engng Fract Mech 2019;209:228–44.

[44] Wang Y, Zhang H, Lin H, Zhao Y, Liu Y. Fracture behaviour of central-flawed rock plate under uniaxial compression. Theor Appl Fract Mech 2020;106:102503.

[45] Zhang D, Wu K. Fracture process zone of notched three-point-bending concrete beams. Cem Concr Res 1999;29(12):1887–92.

[46] Sun X, Gao Z, Cao P, Zhou C, Ling Y, Wang X, et al. Fracture performance and numerical simulation of basalt fiber concrete using three-point bending test on notched beam. Constr Build Mater 2019;225:788–800.

[47] Zhang H, Fu D, Song H, Kang Y, Huang G, Qi G, et al. Damage and fracture investigation of three-point bending notched sandstone beams by DIC and AE techniques. Rock Mech Rock Engng 2015;48(3):1297–303.

[48] Peng C, Guodong L, Jiangjiang Y, Ming Z, Feng J, Zhimeng Z. Research and application of random aggregate model in determining the fracture behavior of four-point

bending beam with notch. Constr Build Mater 2019;202:276–89.

[49]   Yin Y, Qiao Y, Hu S. Four-point bending tests for the fracture properties of concrete. Engng Fract Mech 2019;211:371–81.

[50]   Ferrero A.M, Migliazza M, Roncella R, Tebaldi G. Analysis of the failure mechanisms of a weak rock through photogrammetrical measurements by 2D and 3D visions. Engng Fract Mech 2008;75(3–4):652–63.

[51]   Hedayat A, Pyrak-Nolte L.J, Bobet A. Precursors to the shear failure of rock discontinuities. Geophys Res Lett 2014;41(15):5467–75.

[52]   Hedayat A, Pyrak-Nolte L.J, Bobet A. Multi-modal monitoring of slip along frictional discontinuities. Rock Mech Rock Engng 2014;47(5):1575–87.

[53]   Zafar S, Hedayat A, Moradian O. Evolution of Tensile and Shear Cracking in Crystalline Rocks Under Compression. Theor Appl Fract Mech 2022;118:103254.

[54]   Zhang N, Hedayat A, Bolaños Sosa H.G, Huamani Bernal R.P, Tupa N, Yanqui Morales I, et al. Fracture properties of the gold mine tailings-based geopolymer under mode I loading condition through semi-circular bend tests with digital image correlation. Theor Appl Fract Mech 2021;116:103116.

[55]   Reu P.L, Toussaint E, Jones E, Bruck H.A, Iadicola M, Balcaen R, et al. DIC challenge: developing images and guidelines for evaluating accuracy and resolution of 2D analyses. Exp Mech 2018;58(7):1067–99.

[56]   Sutton M.A, Orteu J.J, Schreier H. Image correlation for shape, motion and deformation measurements: basic concepts, theory and applications. Springer Science & Business Media; 2009.

[57]   Shirole D, Hedayat A, Walton G. Illumination of damage in intact rocks by ultrasonic transmission-reflection and digital image correlation. J Geophys Res: Solid Earth 2020; 125(7), e2020JB019526.

[58]   Peng J, Wong L.N.Y, Teh C.I. Influence of grain size heterogeneity on strength and microcracking behavior of crystalline rocks. J Geophys Res Solid Earth 2017; 122(2):1054–73.

[59]   Potyondy D.O, Cundall P.A. A bonded-particle model for rock. Int J Rock Mech Min Sci 2004;41(8):1329–64.

[60]   Potyondy DO. A grain-based model for rock: approaching the true microstructure. Proceedings of rock mechanics in the Nordic Countries, edited by C. C. Li, pp. 225–234, Norwegian Group for Rock Mechanics, Kongsberg, Norway; 2010.

[61]   Cundall P.A, Strack O.D. A discrete numerical model for granular assemblies. Geotechnique 1979;29(1):47–65.

[62]   Mao L, Lei Y, Ding L, Wu J, Li L, Yang M, et al. Evaluation of 3D deformation field in siltstone with a pre-existing 3D surface flaw under uniaxial compression using X-ray computed tomography and digital volumetric speckle photography. Measurement 2021;110484.

[63]   Fauchille A.L, Hedan S, Valle V, Pret D, Cabrera J, Cosenza P. Multi-scale study on the deformation and fracture evolution of clay rock sample subjected to desiccation. Appl Clay Sci 2016;132:251–60.

[64]   Huang J.Y, Lu L, Fan D, Sun T, Fezzaa K, Xu S.L, et al. Heterogeneity in deformation of granular ceramics under dynamic loading. Scr Mater 2016;111:114–8.

[65]   Kuruppu M.D, Chong K.P. Fracture toughness testing of brittle materials using semi-circular bend (SCB) specimen. Engng Fract Mech 2012;91:133–50.

[66]   Lim I.L, Johnston I.W, Choi S.K. Stress intensity factors for semi-circular specimens under three-point bending. Engng Fract Mech 1993;44(3):363–82.

[67]   Alvarado M.A, Shah S.P, John R. Mode I fracture in concrete using center-cracked plate

specimens. J Engng Mech 1989;115(2):366–83.

[68]   Wei M.D, Dai F, Xu N.W, Zhao T, Liu Y. An experimental and theoretical assessment of semi-circular bend specimens with chevron and straight-through notches for mode I fracture toughness testing of rocks. Int J Rock Mech Min Sci 2017;99:28–38.

[69]   Aliha M.R.M, Razmi A, Mousavi A. Fracture study of concrete composites with synthetic fibers additive under modes I and III using ENDB specimen. Constr Build Mater 2018;190:612–22.

[70]   Mirsayar M.M, Razmi A, Aliha M.R.M, Berto F. EMTSN criterion for evaluating mixed mode I/II crack propagation in rock materials. Engng Fract Mech 2018; 190:186–97.

[71]   Ghanbari N, Hosseini M, Saghafiyazdi M. Effects of temperature and confining pressure on the mode I and mode II fracture toughness of cement mortar. Theor Appl Fract Mech 2019;104:102361.

[72]   Najjar S, Moghaddam A.M, Sahaf A, Yazdani M.R, Delarami A. Evaluation of the mixed mode (I/II) fracture toughness of cement emulsified asphalt mortar (CRTS-II) using mixture design of experiments. Constr Build Mater 2019;225:812–28.

[73]   Wong L.N.Y, Guo T.Y. Microcracking behavior of two semi-circular bend specimens in mode I fracture toughness test of granite. Engng Fract Mech 2019;221: 106565.

[74]   Anderson T.L. Fracture mechanics: fundamentals and applications. CRC Press; 2020.

[75]   Dehestani A, Hosseini M, Taleb Beydokhti A. Effect of wetting–drying cycles on mode I and mode II fracture toughness of cement mortar and concrete. Theor Appl Fract Mech 2020;106:102448.

[76]   Qiu H, Zhu Z, Wang M, Wang F, Ma Y, Lang L, et al. Study on crack dynamic propagation behavior and fracture toughness in rock-mortar interface of concrete. Engng Fract Mech 2020;228:106798.

[77]   Kuruppu M.D, Obara Y, Ayatollahi M.R, Chong K.P, Funatsu T. ISRM-suggested method for determining the mode I static fracture toughness using semi- circular bend specimen. Rock Mech Rock Engng 2014;47(1):267–74.

[78]   Zhang N, Hedayat A, Perera-Mercado Y, Bolanos Sosa H.G, Tupa N, Yanqui Morales I, et al. Including class F fly ash to improve the geopolymerization effects and the compressive strength of mine tailings-based geopolymer. J Mater Civ Engng 2022. https://doi.org/10.1061/(ASCE)MT.1943-5533.0004465.

[79]   Pop O, Meite M, Dubois F, Absi J. Identification algorithm for fracture parameters by combining DIC and FEM approaches. Int J Fract 2011;170(2):101–14.

[80]   Méité M, Pop O, Dubois F, Absi J. Characterization of mixed-mode fracture based on a complementary analysis by means of full-field optical and finite element approaches. Int J Fract 2013;180(1):41–52.

[81]   Sharafisafa M, Aliabadian Z, Shen L. Crack initiation and failure of block-in-matrix rocks under Brazilian test using digital image correlation. Theor Appl Fract Mech 2020;109:102743.

[82]   Aliabadian Z, Sharafisafa M, Tahmasebinia F, Shen L. Experimental and numerical investigations on crack development in 3D printed rock-like specimens with pre-existing flaws. Engng Fract Mech 2021;241:107396.

[83]   Diakhate M, Angellier N, Pitti R.M, Dubois F. On the crack tip propagation monitoring within wood material: Cluster analysis of acoustic emission data compared with numerical modelling. Constr Build Mater 2017;156:911–20.

[84]   Angellier N, Dubois F, Pitti R.M, Diakhaté M, Loko R.S.A. Influence of hygrothermal effects in the fracture process in wood under creep loading. Engng Fract Mech 2017;177:153–66.

[85]   Venzal V, Morel S, Parent T, Dubois F. Frictional cohesive zone model for quasi-brittle fracture: Mixed-mode and coupling between cohesive and frictional behaviors. Int J Solids Struct 2020;198:17–30.

[86]   Lin Q, Labuz J.F. Fracture of sandstone characterized by digital image correlation. Int J Rock Mech Min Sci 2013;60:235–45.

[87]   Kramarov V, Parrikar P.N, Mokhtari M. Evaluation of fracture toughness of sandstone and shale using digital image correlation. Rock Mech Rock Engng 2020; 53(9):4231–50.